Ionic wind produced by positive and negative corona discharges in air

Éric Moreau, Pierre Audier, Nicolas Benard

Ionic wind produced by positive and negative corona discharges in air

Eric MOREAU[1]∗, Pierre AUDIER[1], Nicolas BENARD[1]

[1] University of Poitiers, Pprime institute, CNRS, ISAE-ENSMA

Téléport 2, BP 30179, 86962 Futuroscope, France

∗ corresponding author : eric.moreau@univ-poitiers.fr

Abstract

In this experimental study, we aimed at better understanding the electrohydrodynamic phenomena occurring inside positive and negative point-to-plate corona discharges in atmospheric air. First, electrical and optical measurements allowed us to observe the different discharge regimes according to the voltage polarity; the Hermstein's glow regime and then the breakdown streamer one in the case of a positive corona, and the Trichel pulse regime and then the pulseless one for the negative corona. More, we highlighted that the discharge current always follows the theoretical Townsend's expression, except in one case. Indeed, for the positive corona, the discharge current starts to evolve linearly with the voltage when the streamer regime appears. Secondly, the time-averaged and time-resolved velocity of the ionic wind has been characterized by high speed particle imaging velocimetry. We observed that when the high voltage is switched on, a jet starts from the needle and then its moves toward the plate, resulting in a wall-impinging jet with a vortex ring. Moreover, we highlighted that a negative corona discharge produces a steady ionic wind with weak velocity fluctuations. On the contrary, the positive discharge induces a faster ionic wind, showing that it is more efficient than the negative discharge in ionic wind production, more especially when the breakdown streamer regime appears. However, the presence of streamers results in an unsteady flow with strong velocity fluctuations. Finally, we can affirm that, whatever the polarity of the high voltage, the ionic wind jet is steady when the discharge current is continuous and it becomes unsteady when current pulses are added to the current continuous component.

I. Introduction

When a high potential difference is applied between two electrodes in atmospheric air, ionization of the air molecules around the thinnest electrode induces a corona discharge. Due to the electric field, these ions are submitted to Coulomb force, resulting in their motion from the active electrode toward the grounded collecting one. The set of all these Coulomb forces results in a volume electrohydrodynamic (EHD) force occurring inside the discharge. Hence, in the electrode gap, many collisions between ions in motion and neutral air molecules take place, resulting in a momentum transfer that produces a gas flow, which is usually called “ionic wind”.

Important studies on the physics of corona discharges started at the end of the 19th century[1,2] and continued throughout the 20th century[3–19]. Although they involve complex electrical, chemical and mechanical phenomena, they are easy to enforce. Therefore, they are used in numerous engineering applications, such as ozone production[20,21], reduction of gaseous pollutants[22,23], surface treatment[24], assisted-combustion[25,26], electrostatic precipitation[27–29] and thrust production[30,31] for instance.

In the present paper, we focus on the electrohydrodynamic phenomena occurring inside corona discharges in atmospheric air. The first publication dedicated to this subject is the one of Chattok[2] in 1899, but we can say that theory of EHD in gas started with the well-known publication of Robinson[32] in 1961 that investigated the ability of corona discharges to perfect blowers in absence of any moving mechanical part. More recently, for about 10 years, several others research groups have been studying corona discharges, with the aim at increasing the electric wind velocity, the resulting flow rate and the electromechanical efficiency of such devices[33–37]. However, only few studies have been devoted to a better understanding of the physical phenomena occurring inside the discharge and the complex plasma-gas interaction.

Hence, in the present paper, we propose to detail the ionic wind produced when the discharge is ignited, and to compare negative and positive coronas. For that purpose, we have developed a multi-metrology experimental bench including electrical measurements, iCCD visualizations and time-resolved particle image velocimetry.

II. Experimental Setup

In this study, we aim at characterizing the properties of positive and negative point-to-plane corona discharges. Thus, a high voltage (HV) is applied between a needle and a grounded plane electrode. Both electrodes are made of stainless-steel and are separated by a gap of 25 mm (Fig. 1). The needle electrode is 60 mm-long and has a tip having a curvature radius equal to 100 µm. The plane electrode has a disk shape with rounded edges and a diameter of 80 mm. Its thickness is equal to 5 mm. The high voltage is generated by a HV amplifier (Trek 30 kV/40 mA) having a slew rate of about 600 $V.\mu s^{-1}$ and is measured with a probe (North StarPVM-1, 500 MHz). The discharge current waveform is visualized with a second probe (Lecroy, PP018, 500 MHz, 10 pF) that measures the voltage across a 1 kΩ resistor set between the plate and earth. All the signals can be simultaneously recorded with a digital oscilloscope (Lecroy HDO6054, 500 MHz, 2.5 $GS.s^{-1}$). All the experiments are realized at atmospheric pressure in a few successive days. Even if temperature and pressure are quite constant during this period (T = 22 ± 2°C and P = 1020 ± 2 hPa), the relative humidity could vary a little bit more (RH = 50 ± 15 %). For all the experiments, the time reference t = 0 corresponds to the beginning of the high voltage rise.

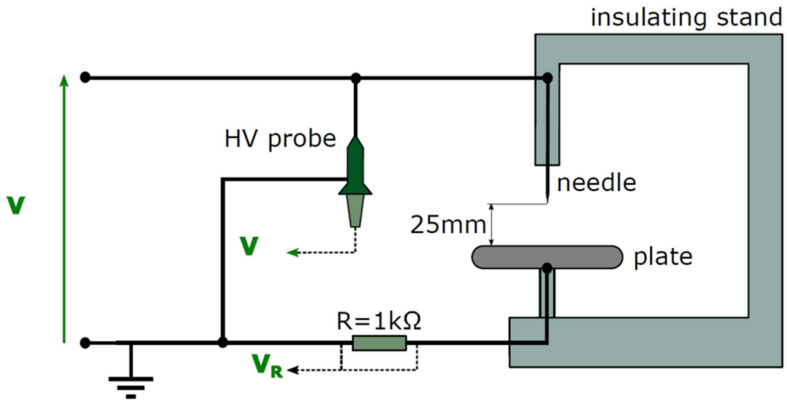

Figure 1. Experimental setup.

Images of the discharge are recorded by a fast gateable iCCD camera (Princeton, Pi-max4 Gen2) with a resolution of 1024×1024 pixels^2 and equipped with a 60 mm objective. The final field of view corresponds to a 39 × 39 mm^2 region (38 µm per pixel). The same trigger source is used to synchronize all the apparatus, including the iCCD camera and the discharge ignition. The time delay between the discharge ignition and the shutter opening the camera is managed using the software of the camera (Princeton Light Field). In this study, two types of snapshots are acquired. On one hand, the shutter of the camera is triggered to open 50 µs before the beginning of the high voltage rise at t = 0 and during 200 µs (t ∈ [-50 µs, 150 µs]). One the other hand, the shutter of the camera is triggered to open 5 ms after the beginning of the high voltage rise, during 2 ms, to observe the morphology of the plasma a few milliseconds after its ignition, when the discharge is well established (t ∈ [5 ms, 7 ms]).

To characterize the ionic wind produced by the discharge, a LaVision time-resolved particle imaging velocimetry (PIV) system is used. The point-to-plane design presented in Fig. 1 is put into a PMMA tank (30 × 80 × 40 cm^3). The air is seeded with dielectric oil droplets (Ondina 915) having a mean diameter equal to 0.3 µm. A 532 nm Nd:YAG laser generator (Continuum Mesa), equipped with a divergent cylindrical lens, is used to provide a laser

sheet that illuminates the particles in the x–y plane, passing through the tip of the needle and the middle of the plate (z = 0). Images are acquired using a high-speed camera (Photron Fastcam SA-Z), with a resolution of 1024 × 1024 pixels^2 and equipped with a 60 mm lens. The resulting images have a size of 30 × 30 mm^2. The acquisition frequency is set to 20 kHz, leading to a time delay of 50 µs between two consecutive images. In total, 3000 vector fields are acquired for each experiment. The produced velocity components is computed using a cross-correlation algorithm with adaptive multi-passes, interrogation windows of 64 × 64 down to 16 × 16 pixels^2 and an overlap set to 50%, leading to a final flow field resolution of one vector every 266 µm.

III. Electrical and optical characteristics

In this section, we aim at characterizing the electrical and optical behaviors of both positive and negative discharges. First, we present current measurements and iCCD visualizations when the discharge is well established (t > 5 ms). Secondly, we focus on the transient regime of the discharge, when the high voltage is switched on (0 ≤ t ≤ 150 µs).

Steady state

Fig. 2 presents the evolution of the time-averaged discharge current versus applied high voltage, in the case of positive and negative coronas (I-V characteristics). Several remarks can be formulated. First, as expected, we can see that the negative discharge results in a higher current than the positive one. For instance, at 14 kV, the positive current is equal to 20 µA when the negative one exceeds 30 µA. Secondly, even if this kind of discharge involves complex phenomena, a simple empirical expression, called Townsend's equation, can be generally used to link the evolution of the current discharge as a function of the applied voltage V[1,3,4]:

$$I = C \times V \left(V - V_0\right) \quad (1)$$

where V is the applied DC voltage, V_0 the ionization threshold value and C a constant depending on the electrode configuration, temperature, pressure and gas composition. As we can see in Fig. 2, this equation allows us to interpolate correctly the experimental measures in the case of the negative corona. On the contrary, for the positive corona, the discharge current follows well Eq. (1) when V is equal or smaller than 14 kV, but when V becomes higher than 14 kV, the current starts to evolve linearly with the voltage. By the past, several authors have already reported some difference between the Townsend's equation and experimental measurements, these differences being observed generally at low current values and depending on the electrode geometry[38,39] or relative air humidity[40]. However, to our knowledge, it is the first time that this kind of behavior is clearly reported. Hence, in order to identify the reasons why the positive current suddenly increased when V reached 14 kV, we decided to visualize the discharge with a iCCD camera and to record the discharge current versus time (Fig. 3). These measurements should allow us to precisely characterize the different discharge regimes.

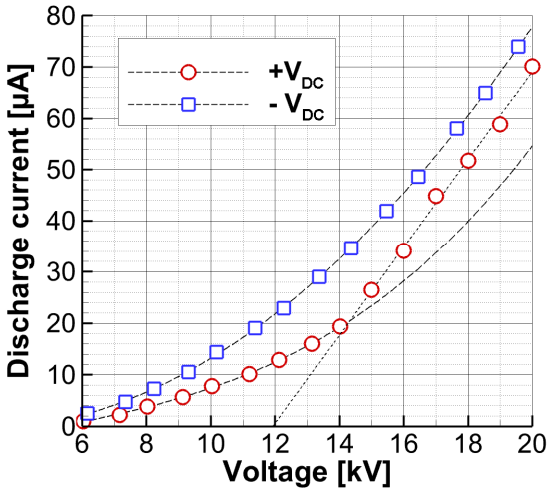

Figure 2. Current versus voltage for positive and negative corona discharges.

First, let us consider the case of the positive corona for which the different discharge regimes have been widely described[9,10,12,13,15,16,19]. Indeed, these studies showed that

different types of corona discharge could be successively observed as the voltage increased: a burst pulse corona composed of small onset streamers, a pulseless Hermstein's glow corona, a breakdown streamer corona and sometimes a diffuse corona before a spark takes place. In our case, for voltages smaller than +14 kV, we observed the stable Hermstein's glow regime[13] characterized by a small ionized region concentrated around the tip of the high voltage electrode (see the case V = +12 kV in Fig. 3). The discharge current is then constant, and equal to a few μA (not visible in Fig. 3 because the current scale is in mA). Over +14 kV, we can see some luminous ionized channels that cross the electrode gap, their number, their thickness and their light intensity increasing as the high voltage increases. Close to the threshold value of +14 kV, only a few pulses are erratically present in the discharge current, but as the applied voltage increases, the amplitude and the repetition rate of the current pulses increase and the time interval between two consecutive current peaks becomes more uniform, around a few kilohertz. For V > +14 kV, the breakdown streamer regime is established, the transition between both regimes occurring around +14 kV. Hence, if we return to Fig. 2, we can assume that the measured current fits Eq. (1) when the discharge is glow. However, when the breakdown streamer appears, the pulsed component of the current which is added to the DC one, results in a shift of the total current compared to the Townsend's equation.

In the case of the negative discharge, different regimes have been also reported in literature, often by the same authors than for the positive coronas. However, the work of Trichel on negative coronas is certainly the most known[7]. Hence, when the discharge ignites, we have first a Trichel pulse corona, and then a pulseless corona before the transition to spark. This is verified in our experimental conditions; we have been able to observe some current peaks for voltage down to -6 kV (not shown here), but when the voltage magnitude

is increased (*i.e.* V < -6 kV), the current is fully constant with time. Looking at the iCCD visualizations (Fig. 4), we can see that the light emitted by the negative discharge is concentrated around the tip of the active electrode, where the discharge is active. Furthermore, the size of this luminous region lightly grows as the voltage increases.

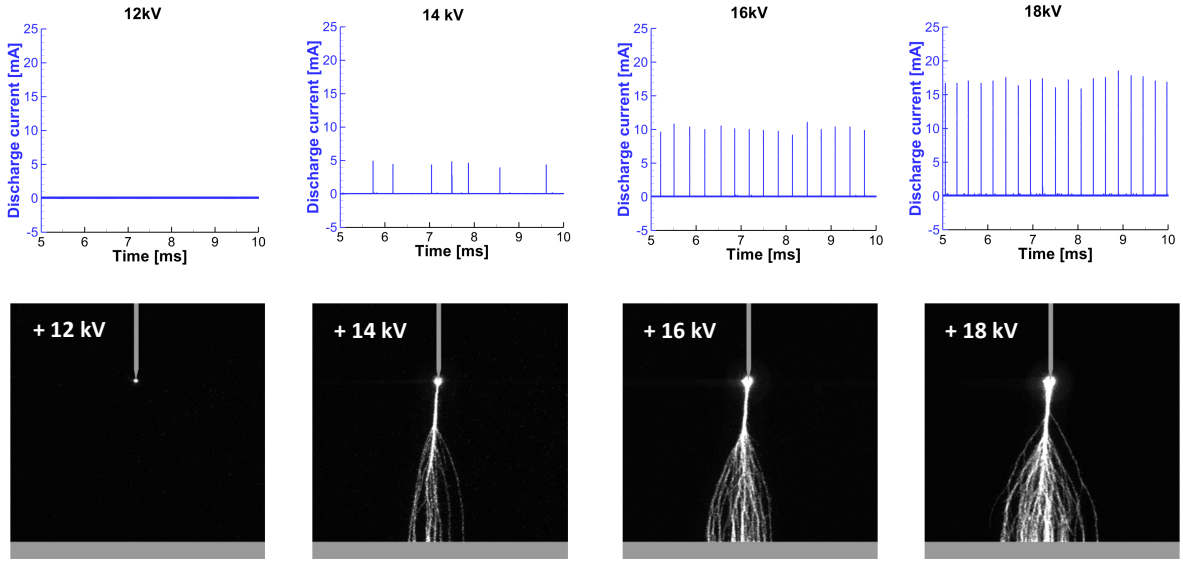

Figure 3. Discharge current versus time and corresponding iCCD snapshots for a positive corona discharge, for voltages from +12 kV to +18 kV. For the iCCD acquisitions, the camera shutter is opened for t ∈ [5 ms, 7 ms]. The electrodes appear in grey, with an electrode gap of 25 mm.

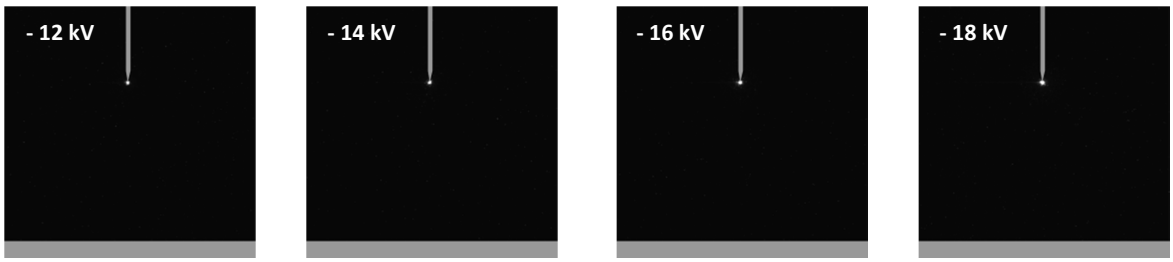

Figure 4. ICCD snapshots of a negative discharge, for voltages from - 12 kV to -18 kV. The camera shutter is opened for t ∈ [5 ms, 7 ms]. The electrodes appear in grey, with an electrode gap of 25 mm.

Transient state

To provide a better understanding of the discharge behavior when the voltage is switched on, electrical and optical measurements are realized. In this case, the shutter of the camera is opened during 200 µs (t ∈ [-50 µs, +150 µs]) to focus on the discharge ignition. In addition, the time evolution of both high voltage and current is simultaneously recorded.

ICCD snapshots are presented in Fig. 5 for positive voltages ranging from +12 kV to +16 kV. When the high voltage starts rising (t = 0), onset streamers start to grow from the tip of the point electrode. The length, the light intensity and the number of ramifications of those streamers increase as the high voltage increases. When the applied voltage reaches +14 kV, the streamers become long enough to cross the inter-electrode gap, reaching the plane. We can notice that these onset streamers are different compared to the breakdown streamers observed for steady state (see Fig. 3). Indeed, the spatial organization of these streamers that occurs during the high voltage drop are similar to the ones observed with a pulsed corona[41]. By looking at the evolution of the corresponding discharge current (Fig. 5), one can notice that when the high voltage starts rising, the discharge current has two components. First, a bump with a plateau of 1 mA in magnitude regardless of the voltage and corresponding to the capacitive component. Knowing that the voltage slope is equal to 600 V/µs, we find an equivalent capacitance equal to about 2 pF. The duration of this plateau corresponding to the time during which the voltage rises with a constant slope of 600V/µs, it ranges from less than 10 µs at +12 kV to about 20 µs at +16 kV. After the plateau, the capacitive current decreases because the slope of the voltage diminishes. Added to this capacitive component, one can see a pulse component, that corresponds to the discharge current. On these current curves, there is always a first small current peak of about 2 mA in magnitude at t ≈ 7 µs. This phenomenon is fully reproducible and corresponds to the ignition of one or several onset streamers. From + 14 kV, the transition from the stable glow regime

to the breakdown streamer one occurs and a second current peak takes place at $t \approx 15$ µs. The magnitude of this peak is higher than the one in the steady state for the same voltage value (see Fig. 3), meaning that this second current peak does not correspond to the first breakdown streamer of the steady state.

In the case of a negative high voltage, otherwise, there is neither current peak, neither streamer during the discharge ignition (Fig. 6). The only difference compared to the iCCD views of Fig. 4 is that the light emitted by the discharge is stronger and the region of emission is wider, because the ionization rate is higher due to the voltage drop.

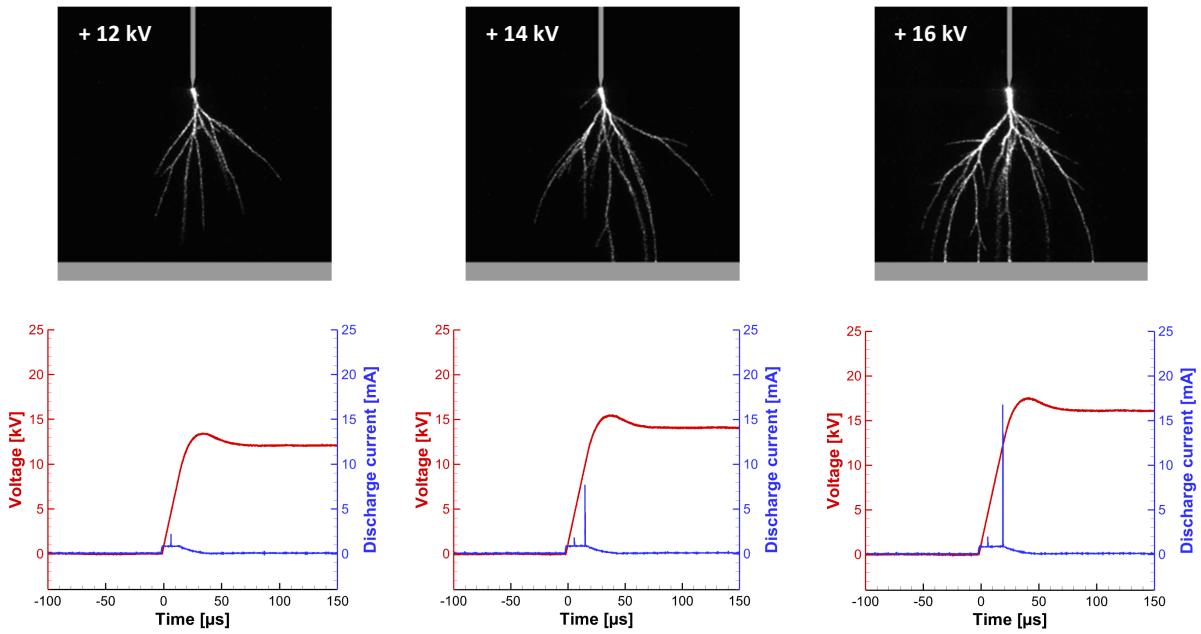

Figure 5. ICCD snapshots of the positive discharge ignition ($t \in [-50$ µs,150 µs]) and corresponding discharge current versus time, for different positive voltage values.

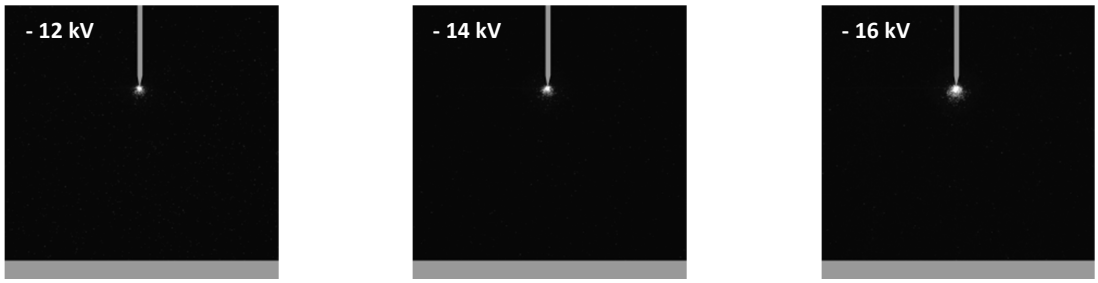

Figure 6. ICCD snapshots of the negative discharge ignition ($t \in [-50$ µs, 150µs]) for different negative voltage values.

IV. Characterization of the produced ionic wind by PIV

After characterizing electrical and optical properties of both positive and negative coronas, we focus now on the discharge hydrodynamics, that is to say the produced ionic wind. First, we present time-averaged velocity measurements, and then we deepen this work by a time-resolved characterization of the ionic wind, from its ignition at t = 0 to its steady state.

Steady state

Fig. 7 illustrates the velocity fields for positive and negative corona discharges, for different voltage values. The needle is located at x = 0 and y = 0 when the plane electrode is located at x = 25 mm. Fig. 8 presents velocity profiles extracted from the previous velocity fields, at x = 5 mm (Fig. 8a) and x = 12.5 mm (Fig. 8b) for a positive discharge to the left, and for a negative one to the right. Several interesting features can be underlined. First, the topology of the flow produced by a positive discharge is fully different compared to the one of a negative discharge. For the negative corona, the maximum velocity is concentrated in a region close to the tip and this region grows and spreads progressively toward the plate when the high voltage is increased (Fig. 7). More, the velocity decreases along the vertical axis X. This feature means that the negative space charge, which is at the origin of the EHD force, is located in front of the tip, in a region which is limited to a few millimeters (even at -16 kV). This can be confirmed by the iCCD images of Fig 4. For the positive corona discharge, the voltage effect is fully different. Up to +12 kV, the region of maximum velocity is located near the point. From +14 kV, when the breakdown streamer regime appears, the mean velocity becomes constant along the x axis, meaning that the mean positive space charge is nearly constant between both electrodes. This highlights the key role of streamers in the EHD phenomenon. To our knowledge, it is the first time that this type of positive ionic wind topology is reported and that a link is experimentally established between streamers and

EHD phenomena. If we look more closely at the velocity profiles of Fig. 8, we can see that the positive discharge leads to a thinner and faster jet compared to the negative discharge, whatever the high voltage value is. Overall, for the positive corona, there is a high velocity gain (from 5 to 7.5 m/s at x = 5 mm) when the high voltage goes from +12 kV to +14 kV, confirming the significant effect of the streamers on the time-averaged velocity of the ionic wind. The physical phenomena that explain this behavior have been highlighted and described in another paper that has been recently submitted for publication[42] . Then, in the present paper, we cannot give all the results presented in the other paper. However, we can say that the velocity gain is due the electrical charge that remains after the propagation of secondary breakdown streamers.

To conclude, we can affirm that the positive discharge is more efficient than the negative one in ionic wind production, whatever the voltage is. For instance, at +8 kV and +16 kV, the maximum velocities are equal to 4.4 and 7.9 m/s for current of 4 and 34 µA, respectively. For a negative discharge at the same voltage values, with higher currents (6.5 µA and 45 µA, respectively), the maximum velocities are limited to 2.8 and 5.9 m/s. On the other hand, Fig. 9 shows that the appearance of streamers results in a unsteady flow. Indeed, for negative coronas (at -12 kV and -16 kV), the RMS values of the velocity is limited to a few percent of the time-averaged velocity. For positive coronas, it is also the case at +12 kV. However, at +16 kV, the RMS values reaches 0.1 in the electrode gap, where the discharge occurs. This means that the ionic wind flow is steady when the current is constant and that there are strong velocity fluctuations, resulting in a unsteady ionic wind jet when the discharge regime is the breakdown streamer one.

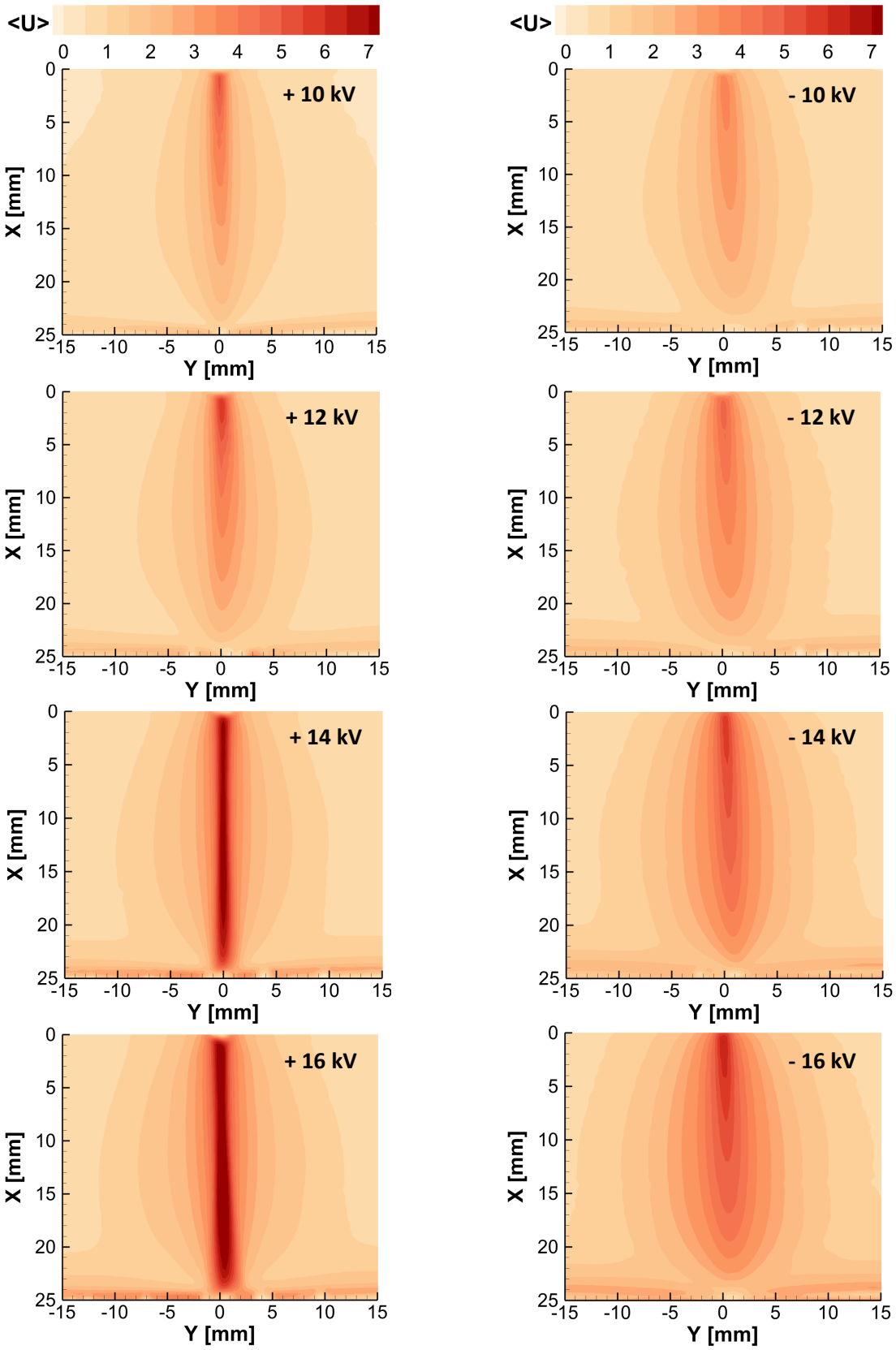

Figure 7. Velocity fields for positive and negative corona discharges, for different voltage values. The needle is located at x = 0 and y = 0 when the plane electrode is located at x = 25 mm.

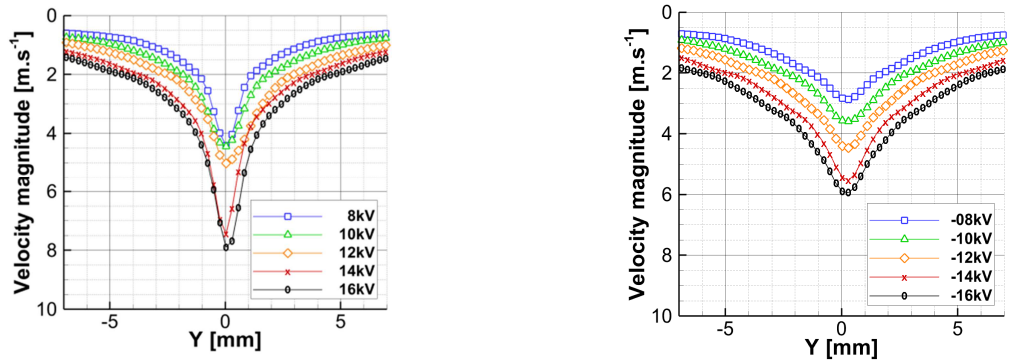

(a)

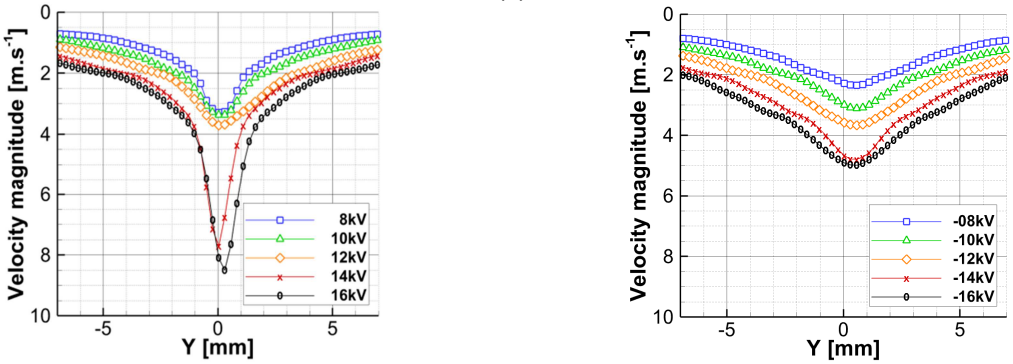

(b)

Figure 8. Velocity profiles at x = 5 mm (a) and x = 12.5 mm (b) for positive (left) and negative (right) corona discharges.

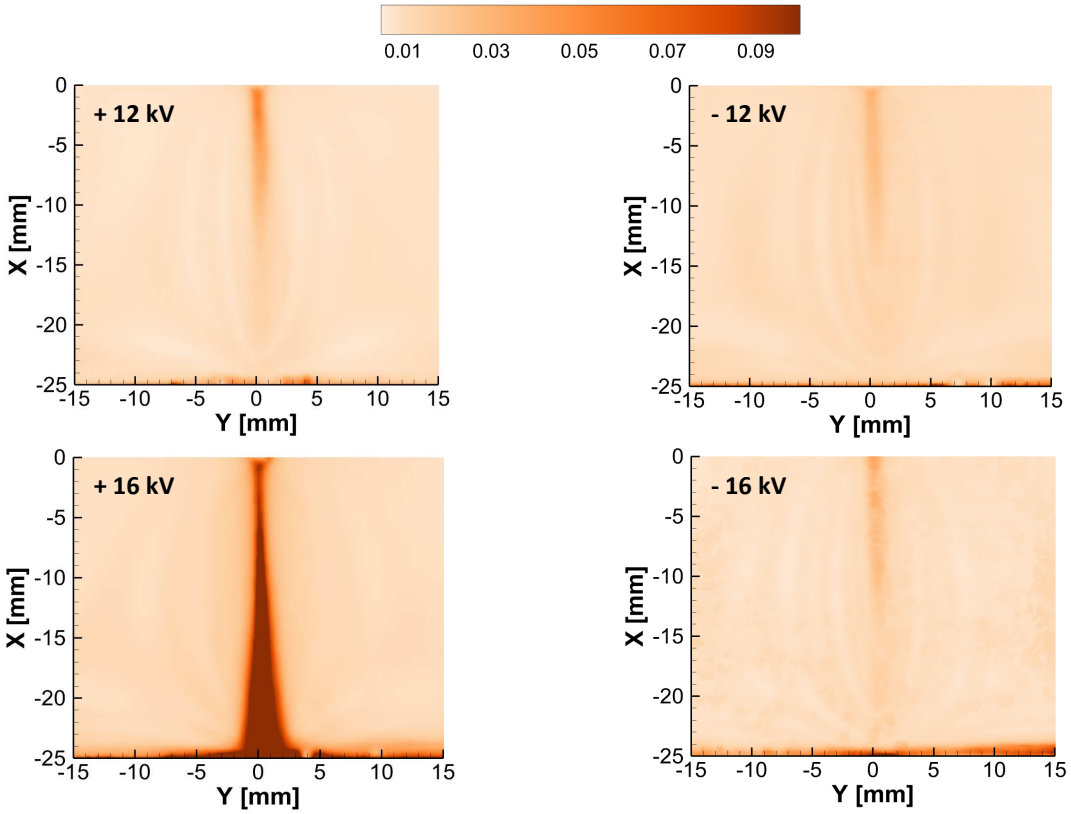

Figure 9. RMS velocity fields for positive (left) and negative (right) discharges, at 12 kV and 16 kV.

Transient state

After a time-averaged analysis, we aim now at characterizing the time-resolved EHD flow when the discharge is switched on. Fig. 10 and Fig. 11 presents the results for +16 kV and -16 kV, respectively. For both figures, the left column corresponds to instantaneous velocity vector fields at different times (t = 1, 2, 4, 8 and 12 ms, the high voltage being switched on at t = 0). On the middle, there are the velocity fields of the vertical component (along X) at the same times. Finally, on the right, we plotted the profiles of the vertical velocity component versus X. These both figures allow us to observe the temporal evolution of the ionic wind topology at the moment when the discharge starts to occur. They reveal that the EHD phenomena during this period are fully different in positive and negative coronas.

In the case of a positive corona, a thin jet starts from the needle with a velocity higher than 5 m/s, 1 ms after the discharge ignition. Then the jet progresses rapidly toward the plane and reaches it in a few milliseconds, resulting in a wall-impinging jet with two vortices that rotates in opposite directions. This underlines that a three-dimensional axisymmetric annular vortex is developing against the wall. If we observe the velocity profiles, we can see that the maximum ionic wind velocity of about 8 m/s is reached at t = 4 ms. More, these profiles show that the velocity distribution is not homogeneous in the electrode gap, highlighting that the ionic wind jet is unsteady because the presence of streamers.

The results obtained with the negative corona confirms those of Fig. 7. Indeed, the ionic wind jet produced when the negative voltage is applied is wider and slower. Moreover, the vertical velocity profiles show that the velocity is nearly constant between the needle and the jet front. This demonstrates and confirms that the ionic wind produced by a negative corona is more steady than the one induced by a positive corona.

To conclude this analysis, we plotted the position of the jet front versus time for two voltage values (Fig. 12). If we look at Fig. 12a (voltages of ±16 kV), we can see that the jet propagation is faster in the positive corona; it reaches the plate wall in 6.6 ms when the negative corona jet needs 10 ms. Moreover, for the positive discharge, the jet propagation velocity is higher in the first millisecond (it is equal to 6.6 m/s) and then it slightly decreases with time due to the presence of the plate wall. On the contrary, the ionic wind jet induced by the negative corona propagates slowly during the first millisecond (velocity of 2.6 m/s) and then its velocity increases and remains constant. We can observe the same behavior at ±8 kV with a smaller jet velocity propagation, the time needed to reach the plate being equal to 14 ms and 18 ms for positive and negative coronas, respectively.

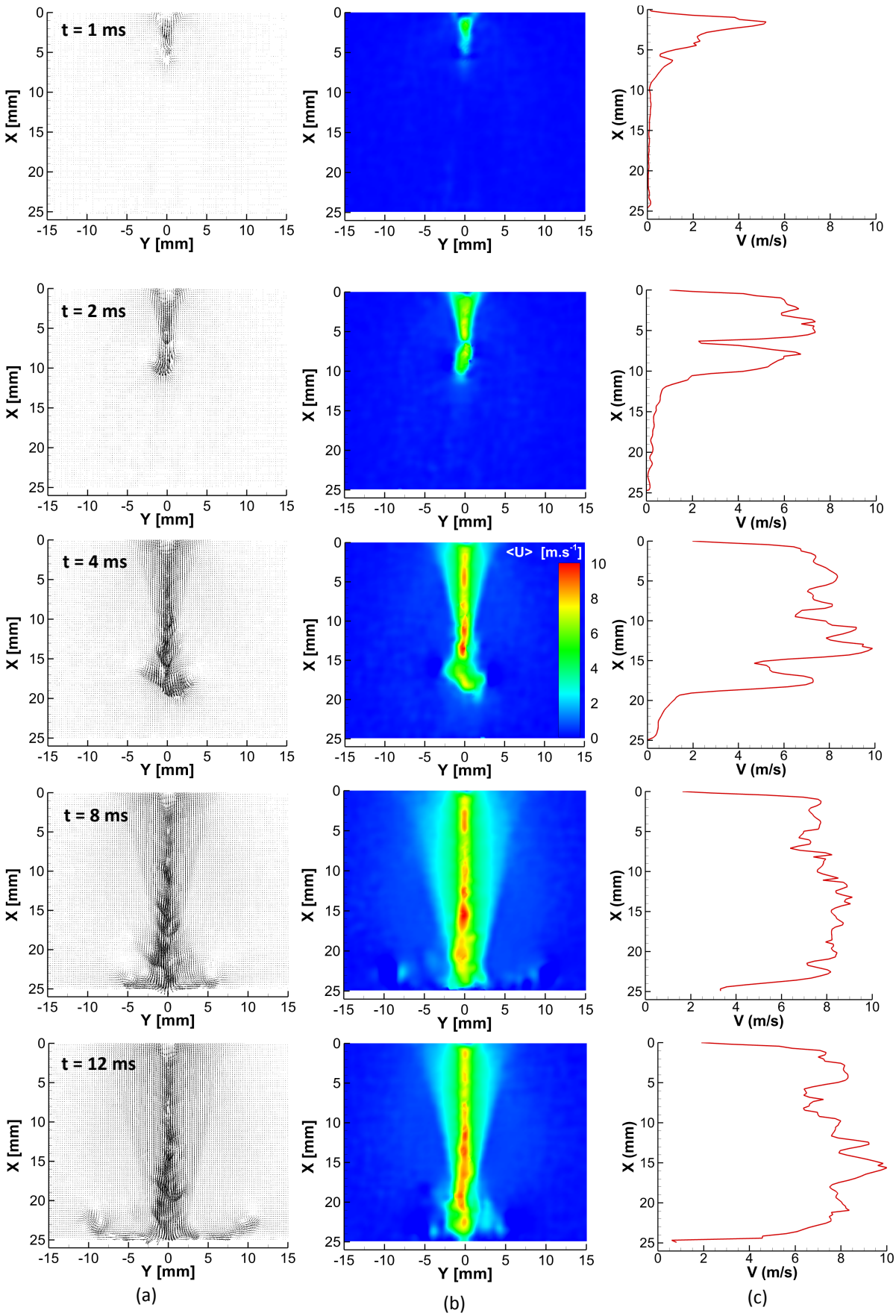

Figure 10. Instantaneous velocity vector fields (a), fields of the vertical velocity component (b) and profiles of the vertical velocity component versus X at t = 1, 2, 4, 8 and 12 ms. The positive high voltage of + 16 kV is switched on at t = 0.

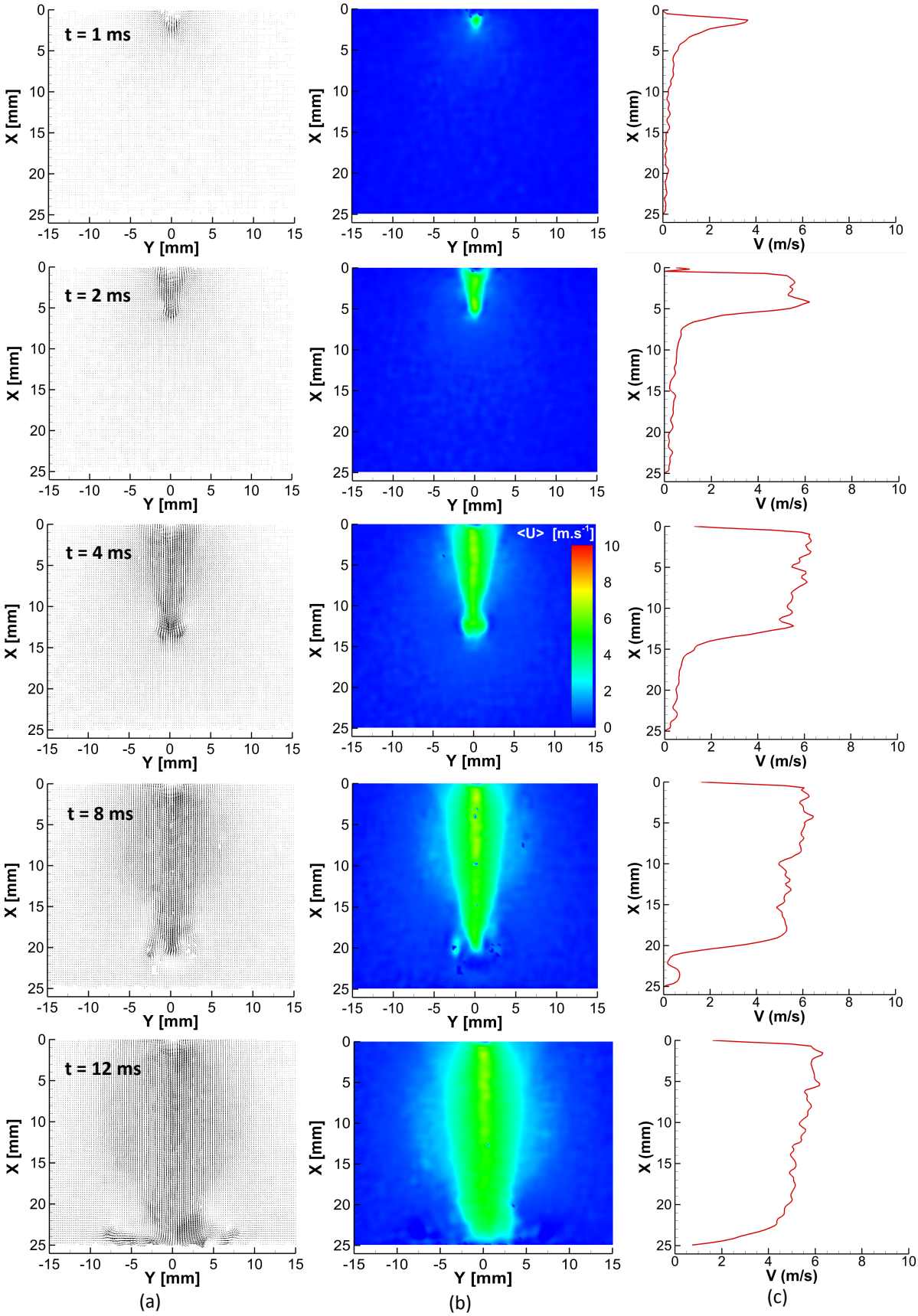

Figure 11. Instantaneous velocity vector fields (a), fields of the vertical velocity component (b) and profiles of the vertical velocity component versus X at t = 1, 2, 4, 8 and 12 ms. The negative high voltage of - 16 kV is switched on at t = 0.

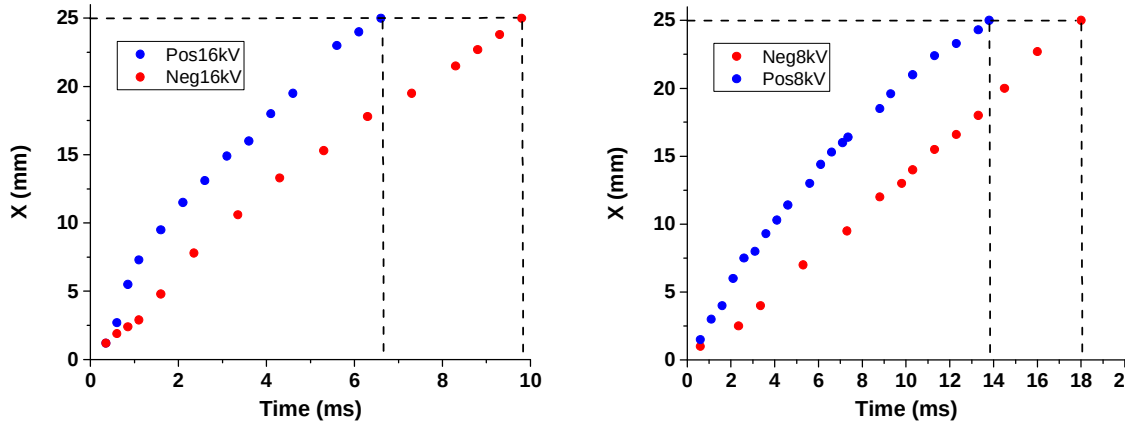

(a) (b)

Figure 12. Position of the jet front versus time for positive (blue circles) and negative corona (red circles) discharges for voltages of ±8 kV (a) and ±16 kV(b).

V. Smoke visualizations of the negative ionic wind

To conclude this paper, we decided to confirm an electrohydrodynamic phenomena which has been recently observed by Mizeraczyk *et al.*[43] in the case of a negative corona discharge. In their paper, the authors studied the first stage of development of the EHD flow produced just after the corona onset with the help of high frequency visualizations. In their experiments, the high voltage was increased slowly from 0 to -8 kV (gap = 25 mm, as in the present study) with a slope of 13.5 V/ms in order to induce trains of Trichel pulses. The time-resolved flow images clearly shown that a ball-like flow structure was produced at the needle just after the corona discharge onset and that the EHD flow evolved like a mushroom-like structure moving towards the grounded electrode. Moreover, they demonstrated that every train of Trichel pulses resulted in a mushroom-like minijet. This result was very important because it highlighted that transient and fast electrical phenomena in a corona discharge (such as Trichel pulses) directly affected the dynamics of the produced flow.

In our case, visualizations of the ionic wind are realized just after the corona discharge onset, at -6 kV and -8 kV in order to be in the same voltage range than in[43] (Fig. 13). Let us

consider the first case at -6 kV (Fig. 13a). When the voltage is switched on, we can see a zone around the needle in which a part of the particles has disappeared (t = 5 ms). In fact, it seems that the high air ionization when the voltage is applied (see iCCD views of Fig. 6) results in a repulsion of particles. Then one can observe the development of a mushroom-like jet (t = 16 ms), as in[43]. This jet propagates toward the plane and as it expands, a shear layer develops around it, forming one main clockwise vortex on one side and another counter-clockwise vortex on the other side (t = 25 ms). This underlines that a three-dimensional axisymmetric annular vortex is developing around the jet. At t = 30 ms, the jet reaches the plane and the two vortices move away from the point of impact of the jet (t = 43 and 50 ms). This is the main behavior of the jet, but if we look more carefully at the image taken at t = 30 ms, we can see a second mushroom-like minijet (spotted with a yellow narrow), such as in[43]. Unfortunately, these visualizations were not synchronized with current measurements. Thus we cannot correlate the temporal behavior of the discharge current with the one of the flow. However, we know that at -6 kV, the current is equal to a few µA and the discharge is a Trichel pulse corona. Consequently, we can think that this mushroom-like minijet is certainly due to a train of Trichel pulses. Moreover, this is confirmed by the visualizations of Fig. 13b where the voltage is equal to -8 kV and where the discharge behaves like a pulseless corona and no second mushroom-like minijet has ever been observed.

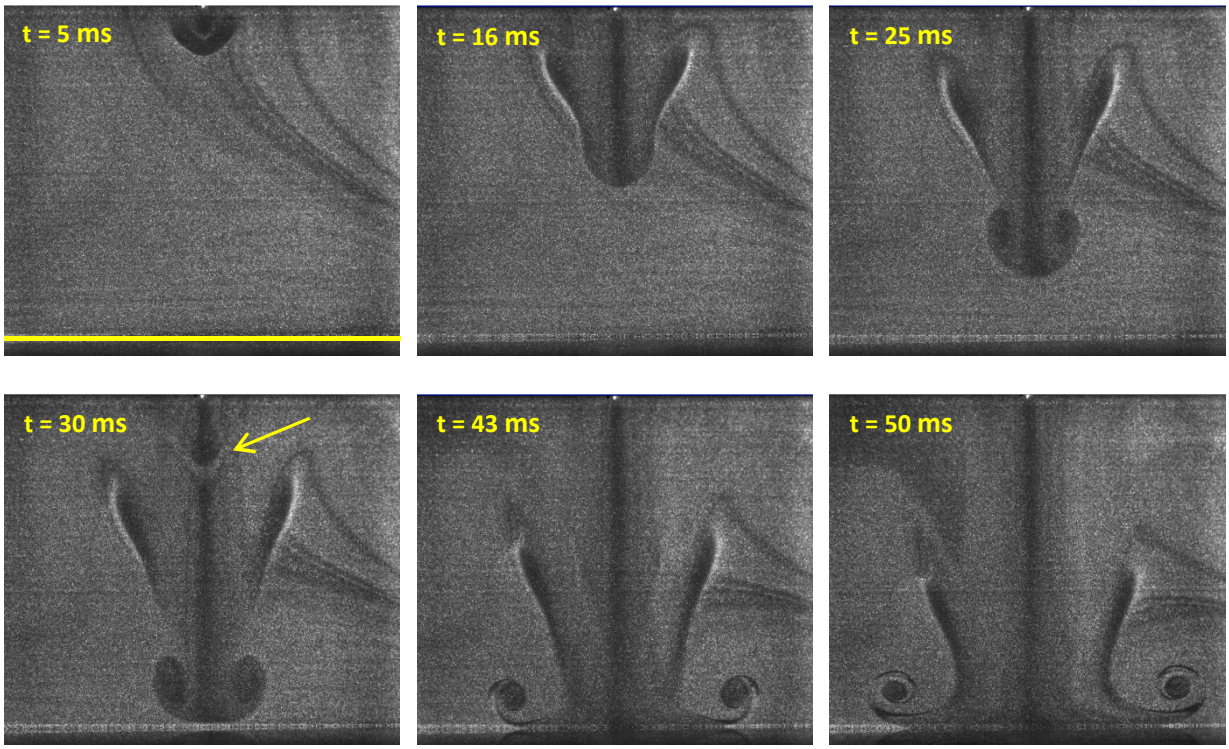

(a)

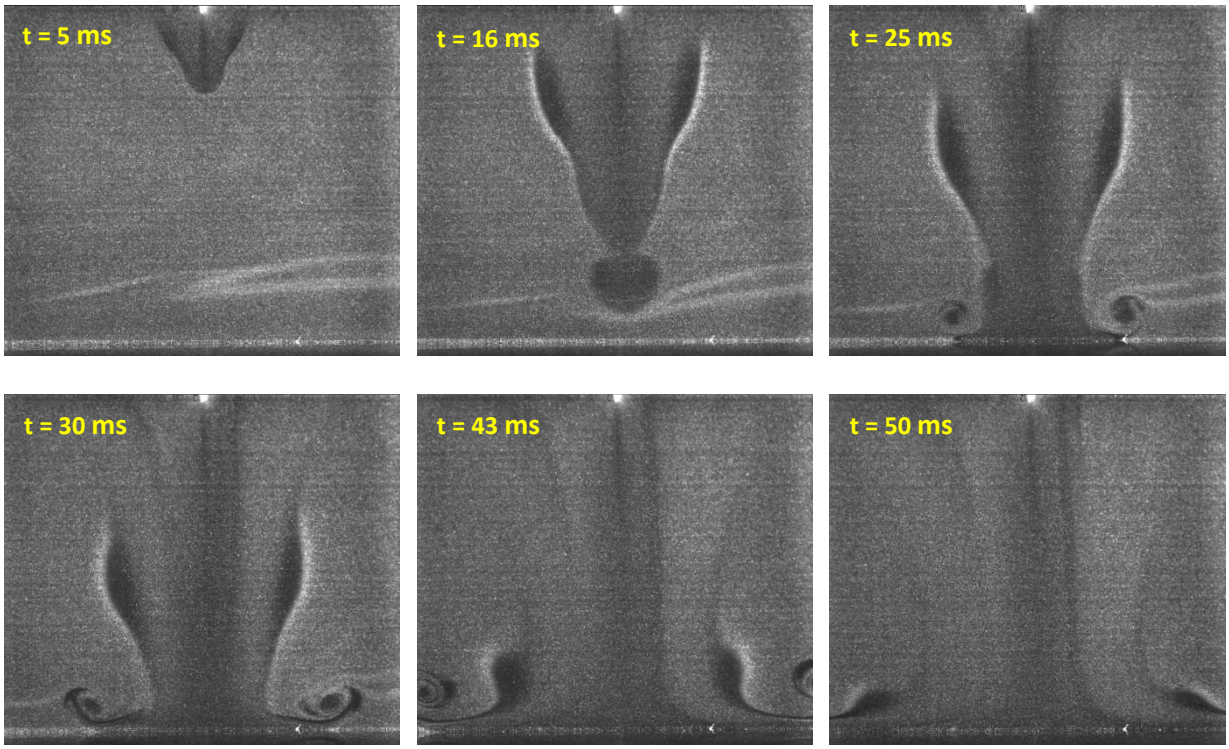

(b)

Figure 13. Instantaneous images of a smoke visualizations of the EHD flow induced by a negative corona discharge at t = 5, 16, 25, 30, 43 and 50 ms for voltages equal to -6 kV (a) and -8kV (b). The negative voltage is switched on at t = 0. The needle is located at the top of the images and the plane electrode appears in yellow in the first image, at the bottom of the images.

VI. Conclusion

In this paper, we studied the ionic wind produced by positive and negative corona discharges and we tried to link its characteristics with the electrical and optical properties of the discharge. For that, we perfected a multi-metrology experimental bench including electrical measurements, iCCD visualisations and time-resolved particle image velocimetry.

First, electrical and optical measurements allowed us to confirm some well-known phenomena concerning the different discharge regimes. In the case of a positive corona, we observed a pulseless Hermstein's glow corona for voltages smaller than +14 kV and then a breakdown streamer corona. For the negative discharge, we observed a Trichel pulse corona only at -6 kV and then a pulseless corona for higher voltage magnitudes. More, on one hand, the I-V curve (mean discharge current versus voltage) could be interpolated correctly by the Townsend's equation in the case of a negative corona whatever the voltage value was. For the positive corona, the measured current follows well the theoretical expression when the voltage was smaller than +14 kV (Hermstein's glow regime) but it starts to evolve linearly with the voltage when the streamer regime appears.

Secondly, the time-averaged velocity of the ionic wind produced by both negative and positive coronas has been characterized by particle imaging velocimetry. For the negative corona, the velocity is maximum inside a region close to the point, this region growing and spreading progressively toward the plate when the high voltage is increased. On the contrary, for the positive corona discharge, the voltage effect is fully different. Up to +12 kV, the region of maximum velocity is located near the point. From +14 kV, when the breakdown streamer regime appears, the mean velocity becomes constant along the x axis, meaning that the mean positive space charge is nearly constant between both electrodes.

Third, we observed the temporal evolution of the ionic wind topology at the moment when the discharge starts to occur and again the results confirmed us that the EHD phenomena during this period are fully different in positive and negative coronas. In the case of a positive corona, a thin jet starts from the needle and then its progresses rapidly toward the plate. It reaches the grounded electrode in a few ms, resulting in a wall-impinging jet with two vortices that rotates in opposite directions. The ionic wind jet produced when a negative voltage is applied is wider and slower.

To conclude, one can affirm that a negative corona discharge produces a steady ionic wind with weak velocity fluctuations because its current is continuous. On the contrary, the positive discharge induces a faster ionic wind, showing that it is more efficient than the negative discharge in ionic wind production, more especially when the breakdown streamer regime appears. However, the presence of streamers results in a unsteady flow with strong velocity fluctuations.

Acknowledgements

This work has been funded by the French Government program INVESTISSEMENT D'AVENIR (LABEX INTERACTIFS, reference ANR-11-LABX-0017-01).

References

1. Warburg, E. Ueber die Spitzenentladung. *Ann. Phys. Chem.* **303,** 69–83 (1899).
2. Chattock, A. P. XLIV. *On the velocity and mass of the ions in the electric wind in air*. *Philos. Mag. Ser. 5* **48,** 401–420 (1899).
3. Zeleny, J. The Discharge of Electricity from Pointed Conductors. *Phys. Rev. Ser. I* **26,** 129–154 (1907).
4. Townsend, J. S. & Edmunds, P. J. LXXXIX. *The discharge of electricity from cylinders and points*. *Philos. Mag. Ser. 6* **27,** 789–801 (1914).
5. Kip, A. F. Positive-Point-to-Plane Discharge in Air at Atmospheric Pressure. *Phys. Rev.* **54,** 139–146 (1938).
6. Kip, A. F. Onset Studies of Positive Point-to-Plane Corona in Air at Atmospheric Pressure. *Phys. Rev.* **55,** 549–556 (1939).
7. Trichel, G. W. The Mechanism of the Negative Point to Plane Corona Near Onset. *Phys. Rev.* **54,** 1078–1084 (1938).
8. Trichel, G. W. The Mechanism of the Positive Point-to-Plane Corona in Air at Atmospheric Pressure. *Phys. Rev.* **55,** 382–390 (1939).
9. Loeb, L. B. Recent Developments in Analysis of the Mechanisms of Positive and Negative Coronas in Air. *J. Appl. Phys.* **19,** 882–897 (1948).

10. English, W. N. Positive and Negative Point-to-Plane Corona in Air. *Phys. Rev.* **74,** 170–178 (1948).
11. Gaunt, H. M. & Craggs, J. D. Electrical and Optical Characteristics of D.C. Corona Discharge. *Nature* **167,** 647–648 (1951).
12. Murphy, B. Positive-Point D.C. Corona. *Nature* **176,** 397–398 (1955).
13. Hermstein, W. Die Stromfaden-Entladung und ihr Übergang in das Glimmen. *Arch. Für Elektrotechnik* **45,** 209–224 (1960).
14. Hudson, G. G. & Loeb, L. B. Streamer Mechanism and Main Stroke in the Filamentary Spark Breakdown in Air as Revealed by Photomultipliers and Fast Oscilloscopic Techniques. *Phys. Rev.* **123,** 29–43 (1961).
15. Loeb, L. B. *Electrical coronas, their basic physical mechanisms*. (1965).
16. Giao, T. & Jordan, J. Modes of Corona Discharges in Air. *IEEE Trans. Power Appar. Syst.* **PAS-87,** 1207–1215 (1968).
17. Sigmond, R. S. The residual streamer channel: Return strokes and secondary streamers. *J. Appl. Phys.* **56,** 1355–1370 (1984).
18. Goldman, M., Goldman, A. & Sigmond, R. S. The corona discharge, its properties and specific uses. *Pure Appl. Chem.* **57,** (1985).
19. Chang, J.-S., Lawless, P. A. & Yamamoto, T. Corona discharge processes. *IEEE Trans. Plasma Sci.* **19,** 1152–1166 (1991).
20. Ono, R. & Oda, T. Dynamics of ozone and OH radicals generated by pulsed corona discharge in humid-air flow reactor measured by laser spectroscopy. *J. Appl. Phys.* **93,** 5876–5882 (2003).
21. Lukes, P., Clupek, M., Babicky, V., Janda, V. & Sunka, P. Generation of ozone by pulsed corona discharge over water surface in hybrid gas–liquid electrical discharge reactor. *J. Phys. Appl. Phys.* **38,** 409–416 (2005).
22. Masuda, S. & Nakao, H. Control of NO/sub x/ by positive and negative pulsed corona discharges. *IEEE Trans. Ind. Appl.* **26,** 374–383 (1990).
23. Kim, H. H., Takashima, K., Katsura, S. & Mizuno, A. Low-temperature NO_x reduction processes using combined systems of pulsed corona discharge and catalysts. *J. Phys. Appl. Phys.* **34,** 604–613 (2001).
24. Ryu, J., Wakida, T. & Takagishi, T. Effect of Corona Discharge on the Surface of Wool and Its Application to Printing. *Text. Res. J.* **61,** 595–601 (1991).

25. Kulacki, F. A. & Boriah, S. Catalytic combustion in a tube with electrical discharge: preliminary measurements of augmented reaction rates. *Nature* **283,** 362–364 (1980).
26. Ju, Y. & Sun, W. Plasma assisted combustion: Dynamics and chemistry. *Prog. Energy Combust. Sci.* **48,** 21–83 (2015).
27. Gilbert, L. A. & George, G. T. Electrical Resistance of Oxide Films formed on the Roll of a Corona Discharge Roll-Type Separator. *Nature* **194,** 1068–1069 (1962).
28. Dascalescu, L. *et al.* Charging of particulates in the corona field of roll-type electroseparators. *J. Phys. Appl. Phys.* **27,** 1242–1251 (1994).
29. Mizuno, A. Electrostatic precipitation. *IEEE Trans. Dielectr. Electr. Insul.* **7,** 615–624 (2000).
30. Christenson, E. A. & Moller, P. S. Ion-neutral propulsion in atmospheric media. *AIAA J.* **5,** 1768–1773 (1967).
31. Moreau, E., Benard, N., Lan-Sun-Luk, J.-D. & Chabriat, J.-P. Electrohydrodynamic force produced by a wire-to-cylinder dc corona discharge in air at atmospheric pressure. *J. Phys. Appl. Phys.* **46,** 475204 (2013).
32. Robinson, M. Movement of air in the electric wind of the corona discharge. *Trans. Am. Inst. Electr. Eng. Part Commun. Electron.* **80,** 143–150 (1961).
33. Rickard, M., Dunn-Rankin, D., Weinberg, F. & Carleton, F. Maximizing ion-driven gas flows. *J. Electrost.* **64,** 368–376 (2006).
34. Moreau, E. & Touchard, G. Enhancing the mechanical efficiency of electric wind in corona discharges. *J. Electrost.* **66,** 39–44 (2008).
35. Tsubone, H. *et al.* Flow characteristics of dc wire-non-parallel plate electrohydrodynamic gas pumps. *J. Electrost.* **66,** 115–121 (2008).
36. Kim, C., Park, D., Noh, K. C. & Hwang, J. Velocity and energy conversion efficiency characteristics of ionic wind generator in a multistage configuration. *J. Electrost.* **68,** 36–41 (2010).
37. Colas, D. F., Ferret, A., Pai, D. Z., Lacoste, D. A. & Laux, C. O. Ionic wind generation by a wire-cylinder-plate corona discharge in air at atmospheric pressure. *J. Appl. Phys.* **108,** 103306 (2010).
38. Ferreira, G. F. L., Oliveira, O. N. & Giacometti, J. A. Point-to-plane corona: Current-voltage characteristics for positive and negative polarity with evidence of an electronic component. *J. Appl. Phys.* **59,** 3045–3049 (1986).

39. Meng, X., Zhang, H. & Zhu, J. (Jesse). A general empirical formula of current–voltage characteristics for point-to-plane geometry corona discharges. *J. Phys. Appl. Phys.* **41,** 065209 (2008).
40. Nouri, H., Zouzou, N., Moreau, E., Dascalescu, L. & Zebboudj, Y. Effect of relative humidity on current–voltage characteristics of an electrostatic precipitator. *J. Electrost.* **70,** 20–24 (2012).
41. Ichiki, R. *et al.* Observing Three-Dimensional Structures of Streamer Discharge Channels. *IEEE Trans. Plasma Sci.* **39,** 2228–2229 (2011).
42. Audier, P., Orriere, T., Benard, N. & Moreau, E. Electrohydrodynamic gas flow in a corona discharge. Submitted to *Scientific Report* .
43. Mizeraczyk, J., Berendt, A. & Podlinski, J. Temporal and spatial evolution of EHD particle flow onset in air in a needle-to-plate negative DC corona discharge. *J. Phys. Appl. Phys.* **49,** 205203 (2016).